Tenth International Conference on Computational Fluid Dynamics (ICCFD10), Barcelona, Spain, July 9-13, 2018

ICCFD10-063

Shape optimisation for the noise induced by the flow over compact bluff bodies

W. J. G. S. Pinto* and F. Margnat*
Corresponding author: florent.margnat@univ-poitiers.fr

* Institut Pprime, Département Fluides, Thermique, Combustion
Université de Poitiers, ISAE-ENSMA, CNRS
Bât. B17 – 6 rue Marcel Doré – TSA 41105
86073 Poitiers Cedex 9, France.

Abstract: Shape optimisation for airframe noise is performed for a cylinder with polygonal cross-section. Acoustic quantities are derived from a hybrid approach, alimented by the incompressible solution of the direct Navier-Stokes equations in 2D; solid domain is defined by a Immersed Boundary Method. Optimisation is done with the Particle Swarm Optimisation (PSO) technique and performed in a cluster where each cost function evaluation is an independent flow simulation. The precision on the 4 main shape parameters is set to 0.001, consistently with the convergence criteria in time, grid and swarm. Optimal shapes for minimum drag and minimum acoustic power are relatively similar. A large range between the optimal shapes is obtained: factor 1.77 for drag and 20 dB for the acoustic power. The reduction of noise is associated with long and bluffer geometries, while the louder flows are associated with highly interacting shear layers obtained with back facing triangles. The fluctuating lift is the major quantity to control noise at fixed length, while the aspect ratio tends to reduce the noise for globally all geometries.

Keywords: Aeroacoustics, Airframe Noise, Shape Optimisation, PSO, IBM.

1 Introduction

The optimisation of a shape for the reduction of the noise generated by a passing flow is performed. The airframe noise is an important source of acoustical discomfort in modern transportation, notably for rear mirrors and landing gears. The basics of the noise mechanism can be reduced to an uniform flow and a cylinder of arbitrary section, described primordially by the interaction of generated vortex street and the solid walls. Directly associated with the fluctuation of aerodynamic efforts, its comprehension is coupled with topics such as vibration and energy harvesting.

The problem of the cylinder wake is secular in aerodynamics and it has been extensively studied since the fundamental works of Strouhal and Karman. Despite many efforts performed for its description, models still relay highly in empiricism [1], and are focused mainly in circular and square cylinders. Qualitative, and most importantly, quantitative estimations of the influence of the shape in the wake structure are extremely sparse.

To look more clearly to the fundamental traits of a geometry that make it quieter or louder, a shape optimisation is performed. Notable applications of optimisation for fluid dynamics problems are available on the literature (see the recent contributions of [2] and [3] for instance), however they are often associated with numerical solution under strong hypothesis or surrogate functions and have aerodynamic quantities as the main objective. Current approach is based on a direct Navier-Stokes calculation, whereas the precision of the technique and its realistic detachment prediction, a low Reynolds regime is imposed. In many experiments such as [4, 5, 6], the frequency associated with lift fluctuations remains the principal peak of the noise spectra at high Reynolds even if the Strouhal number can undergo a slight increase. Thus, the use of low Reynolds regime is relevant not only for the study of the wake dynamics close to the onset of the fluctuations, but also for a greater range of flows.

A robust meta-heuristic optimisation routine based on swarm intelligence, Particle Swarm Optimisation (PSO), is implemented. The hybrid evaluation of the noise production is assessed by an analytical formula derived from the Curle's analogy [7] and serve as the output of the objective function (a complete flow evaluation).

The global optimisation procedure thus combines PSO with DNS embedding IBM associated with an analytical formula which directly estimates acoustic power from aerodynamic quantities. It was described in details in [8]. In the present study, attention is focused on enlarging the range of the outputs introducing a new parametrisation of the shape, which is here based on four vertex connected with straight segments and freely moving on the sides of a rectangle. Moreover, a careful description is included of what the settings are so that global precision is coherent and leads to relatively robust optimisations in spite of errors and uncertainties at each stage (e. g. grid refinement, optimisation convergence...).

The paper is present as follows. Second section contains the description of the solver (2.1), the numerical setup and the mesh and domain independence studies (2.2). On Section 3, the optimisation technique and the parametrized geometry are detailed. Results of the application of the optimisation procedures for optimal drag and noise power are assembled on Section 4. General discussions and conclusion finalize the document on Section 5.

2 Aeroacoustic methodology and qualification

2.1 Acoustic power estimation

An aeroacoustic analogy is used in this study. The hybrid solution is aimed to provide a criteria for the optimisation, on this case, the acoustic power W of the total, tonal noise emission by the flow over a body is selected. It is deduced from Curle's solution for a compact source in 2D, as given by [9]:

$$W = \frac{\pi}{16} d\rho_0 U_\infty^3 \text{ St } \mathrm{M}^2 (2{C'_D}^2 + {C'_L}^2) \tag{1}$$

where W is the acoustic power (integral of the acoustic intensity over the observer circle of arbitrary radius), ρ_0 is the density in the propagation medium, U_∞ is the upstream velocity, d its the main cross section. The Strouhal number St is based on U_∞, d, and the main frequency of lift fluctuations. Noting c_0 the sound velocity, $\mathrm{M} = U_\infty/c_0$. C'_D and C'_L are the period's root mean square (RMS) of the fluctuations of the drag (F_1) and lift (F_2) coefficients, defined per unit length:

$$C_D = \frac{F_1}{\frac{1}{2}\rho_0 U_\infty^2 d} \qquad\qquad C_L = \frac{F_2}{\frac{1}{2}\rho_0 U_\infty^2 d} \tag{2}$$

The flow is numerically predicted by direct solution of the incompressible Navier-Stokes equations (DNS) using incompact3d. The solver uses a 6th order centered finite differences scheme in space (degraded on borders) and 3rd order explicit Runge-Kutta scheme in time. More details are available in [10].

Solid domain is modelled by an Immersed Boundary Method (IBM) [11] where a forcing term $\mathbf{f}$ is added to the momentum equation:

$$\frac{\partial \mathbf{u}}{\partial t} + \mathbf{u}_j \frac{\partial \mathbf{u}_i}{\partial y_j} = -\frac{\partial}{\partial y_j}[p\delta_{ij} - \tau_{ij}] + \mathbf{f} \qquad \text{with} \qquad \mathbf{f}(\mathbf{y},t) = -\epsilon(\mathbf{y}) \left[\omega_n^2 \int \mathbf{u}(\mathbf{y},t)dt + 2\zeta\omega_n \mathbf{u}(\mathbf{y},t)\right] \tag{3}$$

where $\omega_n = 50$ is the natural frequency and $\zeta = 1$ is the damping coefficient of the second order controller that forces a null velocity everywhere ϵ is non zero, values selected from [12]. No interpolation correction is used to adjust the geometry walls. A remarkable advantage of this approach is that the sum of the forcing terms applied to the solid domain gives directly the resulting aerodynamic forces acting on the obstacle, that is, C_D and C_L. Any arbitrary solid shape is modelled with the modification of the ϵ matrix in the same Cartesian grid, an extremely advantageous asset for the use of this technique in optimisation, where hundreds to thousands of geometries must be studied.

2.2 Numerical Setup and Validation

The present analysis is performed with Reynolds number $Re = U_\infty d/\nu$ of 150, where ν is the kinematic viscosity. The small Reynolds number is mandatory so the physics of the problem can be reproduced in a 2D simulation, however, for the wide range of geometries that are considered in the optimisation, there are no warranties that the flow is always well described without the third dimension. For this regime, both drag and lift are close to sinusoidal signals, so the flow periods are defined from consecutive lift peaks. The final simulated period statistics (C_D, C_L and St) are used for the analysis presented on this paper. In order to compute Equation 1, the Mach number is arbitrarily set to 0.1, without any consequence on the comparisons between shapes in the same conditions.

Uniform velocity is set inflow, while a convection condition is set outflow; lateral boundaries are defined with free slip condition. Mesh is uniform in flow direction and stretched in transverse direction, with grid points concentrated in the center. Flow initial condition is uniform and equals inlet velocity, $u_1 = U_\infty$ and $u_2 = 0$, for the complete domain including the solid elements. No disturbance is added, once the transient from the IBM elements are sufficient to give onset to the flow periodicity. A scheme of the domain is presented in Figure 1. Lateral boundaries are fixed at $20d$ for a blockage ratio of 5%, based on [13].

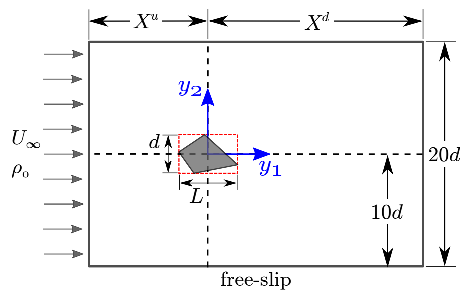

Figure 1: Scheme of numerical domain.

Domain and mesh independence tests are performed for both upstream and downstream distances of the vertical boundaries (X^u and X^d, respectively) and element size (number of grid elements). Not only to quantify the consistency of the numerical setup, this study is also aimed to reduce both memory and time requirements for the use of the DNS simulations for an stochastic optimisation that requires the evaluation of thousands of cases, while correctly representing the physics of the problem.

The tests are performed with an arbitrary symmetrical shape of height d and length $2d$, composed by half ellipse at the leading edge ($y_1 \leq -0.1L$) and two second degree polynomials on trailing edge, enabling C^1 and C^2 continuities with the ellipse. The solid domain is the set of grid points that are inside the selected closed contour, defined by ones on the $\epsilon(\mathbf{y})$ matrix. The use of a non-canonical geometry for this step is justified by the intended use of its conclusions, once there is no restriction of the geometry that is going to be observed when running the optimisation.

2.2.1 Domain convergence

The domains analysis is performed for different streamwise extensions, with a variable number of grid points to maintain the elements' size constant. The number of mesh points in both transverse and flow direction is chosen as a multiple of small prime factors + 1 for a better performance of the spectral solution of the Poisson equation, consequently, they are the parameters that defined the selected test distances. Mesh elements are of size $(\Delta y_1, \Delta y_2) = (1.953, 1.125) \times d/100$ at $y_2 = 0$, and timestep duration is of $\Delta t = 0.0042d/U_\infty$, with a Courant number of $CFL = 0.21$; calculation stops at 40,000 timesteps ($t = 170 \times d/U_\infty$).

Simulations are performed for asynchronous variations of X^u and X^d, being the complementary distance fixed at an arbitrary level issued from previous testing. These evaluations are based on the hypothesis that the effect of the modification of a boundary location is independent of the position of the other for the chosen complementaries ($X^u = 12d$ and $X^d = 18d$). Results are presented on Figure 2 for the variables of interest (mean drag $|C_D|$ and fluctuating lift C'_L). Other aerodynamic quantities present in the aeroacoustical model are also analysed, but not graphically presented here for compactness.

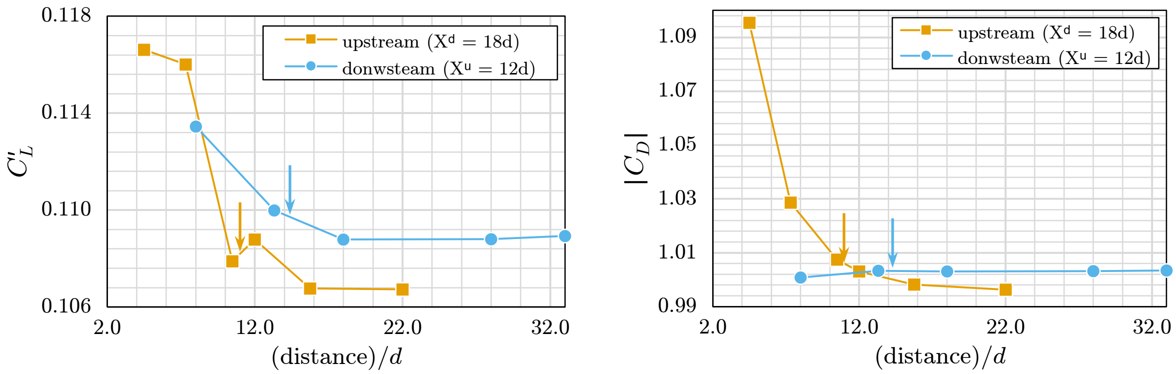

Figure 2: Influence of domain upstream and downstream distances on fluctuating lift and mean drag. Arrows point to the selected configurations.

Asymptotic curves are obtained for both X^u and X^d, similarly to the results for circular section by Posdziech and Grundmann [14]. Simultaneously, it is observed that an increase in those two reduces the levels of fluctuating lift and drag. The order is not similar for mean drag and Strouhal number: they are monotonically increasing for X^u and monotonically decreasing for X^d. According to this tendency, variations of the actual boundaries distances from the section edges caused by the modifications of the length of the geometries in the optimisation procedures are always advantageous, once they are smaller than the value used in the convergence tests ($L \leq 2d$).

Inflow distance has more influence in the flow response due to the modification of upstream conditions in the presence of the obstacle, even at large X^u. The obtained curves confirm that the selected fixed value for the complementary distance are coherent in terms of flow physics.

For a precision of about 1%, the selected values for the final domain are $X^u = 11d$ and $X^d = 14.31d$, what represents a mesh of 1297×513 grid points. Simulations are performed for the selected domain and the final result is compared to the extrema of the domain study, as presented on Table 1.

Table 1: Aerodynamic quantities' errors between the final domain and the most extended boundaries.

case	X^u/d	X^d/d	$\Delta\|C_D\|$	$\Delta C'_L$	$\Delta C'_D$	ΔSt
X^u max	22.0	18.0	-3.2%	-1.2%	-13.5%	-0.8%
X^d max	12.0	33.0	-1.1%	-0.5%	-10.4%	-0.4%

Final domain has higher level for all quantities, as indicated on Figure 2, albeit the discrepancies are relatively small. The fluctuating drag has an elevated offset (order of 10%) provoked by its low order O(-4) and thus has a insignificant influence in the aeroacoustical result. Once the domain is defined, further steps are performed for reducing the calculation time.

2.2.2 Mesh convergence

When comparing the element size, the ratio between number of elements in streamwise and spanwise directions is maintained, thus, the elements are isotropically contracted or expanded. A total of 5 meshes are tested, being number 4 the mesh used on the domain study and number 5 the most refined. The timestep physical duration is modified to guarantee numerical convergence, and the number of timesteps is chosen to achieve at least $225 \times d/U_\infty$ of physical time, within which the comparisons are performed. Figure 3 presents the results for fluctuating lift and mean drag.

For the presented quantities, there is a maximum offset of 1.2% for C'_L and 3.3% for $|C_D|$, when compared to the most refined grid. There is a 8.5% deviation for C'_D and 0.4% for the Strouhal number. The small impact of the mesh refinement can be associated to the flow regime, because once the Reynolds number is small, the flow presents very large boundary layers that are less influenced by small oscillations in the solid

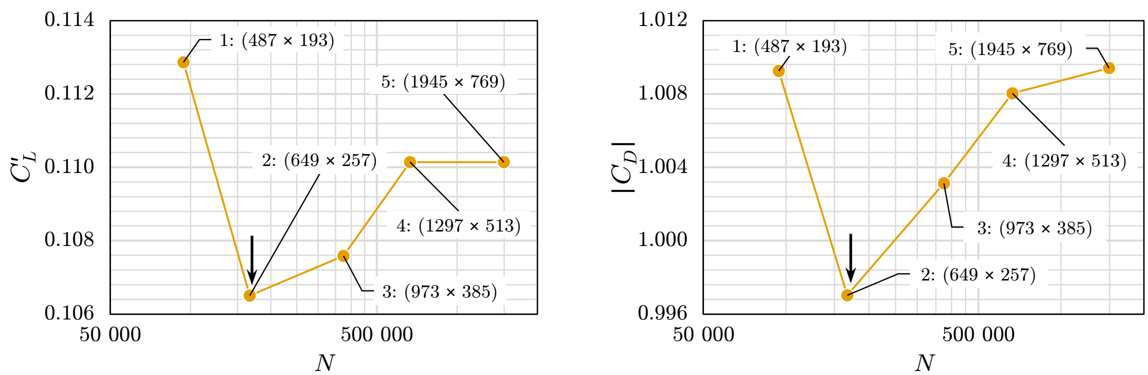

Figure 3: Influence of mesh refinement in fluctuating lift and mean drag. Tags indicate the number of elements in flow and transverse directions, respectively, and arrows point to the selected configuration.

elements size and position. Observed fluctuations may be associated with the modifications of the dynamic of the solid domain by the consistent change in the number of solid points, once the finite difference scheme is unchanged and there are no interpolations on the obstacle wall.

Following the behaviour of the global coefficients, a similarly good result is also obtained when spanwise velocity profiles are compared, as showed on figure 3. The mean and RMS velocity profiles at $y_1 = 0$ of the last 2 simulated periods are presented for meshes 2 and 5.

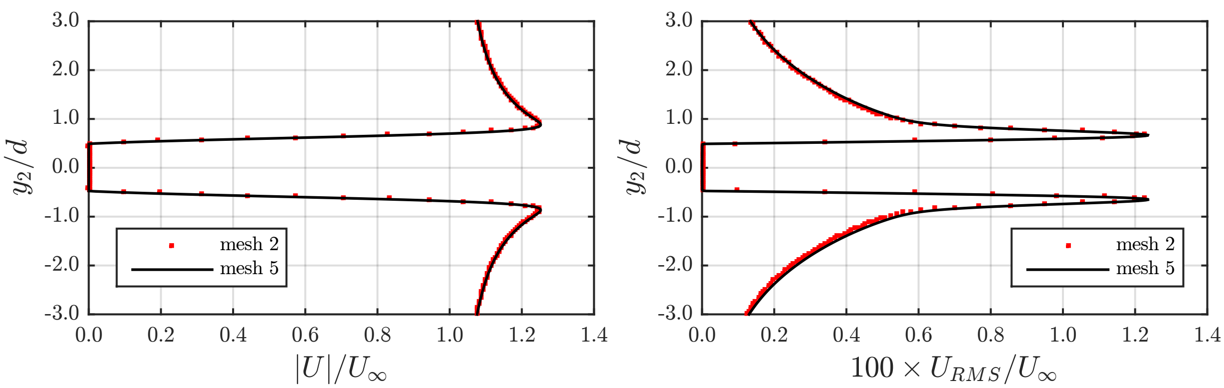

Figure 4: Influence of mesh refinement in mean (left) and RMS (rigth) velocity profiles at $y_1 = 0$.

Profile comparisons at upstream ($y_1 = -5d$) and downstream ($y_1 = +5d$ and $y_1 = +10d$) positions are performed similarly to the analysis executed at the central spanwise axis ($y_1 = 0$). Considering all 4 profiles, there are a maximum deviation of 1% for the mean velocity and of $8 \times 10^{-3} \times U_\infty$ for RMS velocity profiles.

In a search for a compromise between time consumption and physical representativeness, mesh number 2 is selected. For the chosen space discretisation, there are about 25 elements by diameter in y_1 and 50 in y_2. There is a slight loss in accuracy, however, for an equal flow time and CPU conditions, calculation time is reduced to 2.5% of the one obtained with mesh number 5. For 50,000 timesteps, an average CPU time of 2 hours is needed for a single simulation.

Though similar accuracy could be obtained with even coarser meshes, the corresponding geometrical precision would be reduced leading to the fact that relatively large modifications of parameters would be irrelevant for the solver. The consistency of the optimisation depends on the fact that variations of the theoretical geometry are well represented in the solver, even if the difference in the aeroacoustic answer is not significant, respecting the physics of the cost function.

2.2.3 Time convergence

Once the domain and the mesh are fixed, further analysis must be performed to check in time convergence. Figure 5 illustrates drag evolution and the convergence of the period aerodynamic quantities, based on the relative error of the 10 points moving average. A convergence of 0.01% is observed for the quantities of interest at $t = 300 \times d/U_\infty$. The Strouhal number does not oscillate after $t = 150 \times d/U_\infty$, what can be explained by the limits in the technique used for determining it (inverse of a lift period, maximum precision being the duration of a timestep), and obtained errors after that time are either null or of the order of the machine precision.

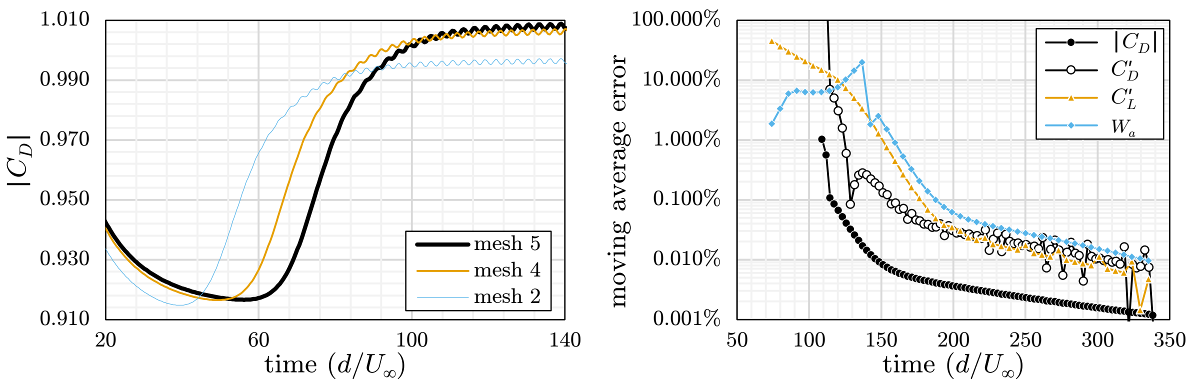

Figure 5: Time evolution of drag coefficient for different meshes (left) and time convergence of mean drag, fluctuating drag and lift and acoustic power for the final domain, with mesh 4 (right).

Convergence in time is also regarded for the different meshing configurations from the previous studies. Apart from differences in time required for the settlement of the periodic wake structure, as noted on Figure 5, there is no significant variation of convergence errors or convergence time as a function of either the domain size or the discretization level.

2.2.4 Validation

Based on mesh and domain independence studies, final mesh ($X^u, X^d = 11d, 14.31d$ and a grid of 649×257 points) is used for a validation procedure against literature values for 40,000 timesteps ($t = 288 \times d/U_\infty$). Simulations are performed with canonical geometries at different lengths and Reynolds numbers. The mean drag of a circular cylinder and RMS lift of rectangular cylinders are compared with literature values [15, 14, 16, 17] and presented on Figure 6.

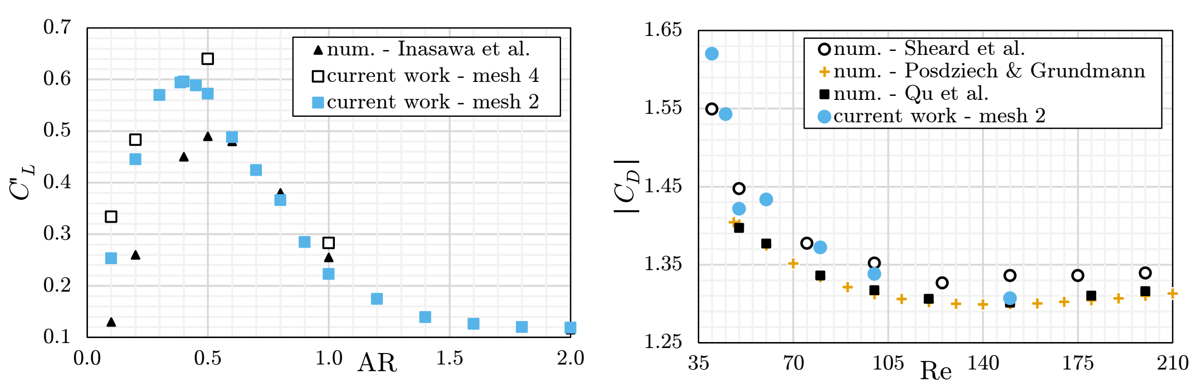

Figure 6: Comparison with literature of the fluctuating lift of a rectangle at different lengths (left) and of the mean drag of circular section at different Reynolds numbers (right).

A positive offset between current results and literature tendency is present in almost all points, at both graphs, and so it is for the Strouhal number and the drag fluctuation (not shown here). The elevated levels are a result of the choices made in the previous sections, where a shorter and coarser mesh would result in higher aerodynamic quantities. Although the limited precision for individual cases characterization, the trends are maintained and there is a global good fit when confronted to literature data.

In summary, considering the performed study and settings, all the results presented here are acknowledgedly slightly over estimated, at the order of 1 to 5%. However, even with the limited accuracy that is obtained, these small oscillations are negligible when confronted to the elevated differences that are searched in an optimisation routine. Once the trends are shown to be respected, the use of the proposed numerical setup is considered adapted to the current application where the results are basically going to be compared with each other.

3 Optimisation framework

Once the solver is well defined, the optimisation algorithm is implemented. As the cost function is relatively expensive, care with the choice of the technique and its settings and the geometry parametrization is taken. Details of those two steps are presented next.

3.1 Optimisation method

Optimisation is performed using the stochastic Particle Swarm Optimisation method, introduced by Kennedy and Eberhart [18]. It is based on the social behaviour of individuals. At each iteration T, the positions of the current best results for the objective/cost function at the individual (p_i) and swarm (g_i) levels are used as targets, along with the previous iteration velocity ($v_{i,T}$). The corresponding vectors from current location ($x_{i,T}$) in the design space are weighted and summed to give the following position ($x_{i,T+1}$). The location of the best values are updated and the process continues until swarm convergence. The considered ratios of each contribution (individual best, global best and last velocity) are regulated by cognitive (c_1), social (c_2) and inertial (c_w) factors, respectively. For the first 2 components, at every iteration and direction, independent and uniformly distributed between [0,1] random factors r_1 and r_2 are used. The later's role is to avoid convergence to local minima and to push the algorithm for further investigation of the design space.

$$x_{i,T+1} = x_{i,T} + c_w v_{i,T} + c_1 r_1 (p_i - x_{i,T}) + c_2 r_2 (g_i - x_{i,T}) \tag{4}$$

The g_{best} topology is used, what means that all particles communicate with the swarm from the beginning to the end of the optimisation. It is a rather robust configuration, but less adapted in the case of several local minima. Particles that leave the design space are simply repositioned to the optimisation domain edge, with no modification in its velocity. More strategies concerning the use of PSO are reported on [19].

Preliminary tests were performed to select the optimisation parameters for a similar test case ([8], symmetrical bluff body composed by 4 Bézier curves). Based on discrete 2D response surfaces and canonical benchmark functions in low dimension (Michalewicz in 2D and 3D), the values of $c_w = 0.6$ and $c_1 = c_2 = 1.2$ are selected for their good success rate at lower number of iterations/function evaluations. Although they vary slightly from the reported best on the literature [20, 19], the selected values were more adapted for the projected response function at a low dimension. Similar analysis were performed with the number of elements in the swarm: for a compromise between the calculation time, that is the number of iterations, and the intended calculation precision, 36 particles are used for each optimisation run (independently of the number of dimensions of the design space). Starting positions are either equally distributed points in the design space (grid of $3 \times 3 \times 2 \times 2$) or randomly distributed using Latin Hypercube Sampling (for 5 degrees of freedom and re-runs).

Maximum number of iterations is fixed at 30, value also based in previous empirical testing, and optimisation stops when swarm stagnation is achieved. The selected criteria for stagnation is the average distance of the particles, quantified by the sum of the Euclidean distances of an arbitrary particle to the other members of the swarm divided by the number of particles; calculation is halted if this value is smaller than 0.001.

The optimisation is performed in a cluster where each flow simulation is single cored, and for every iteration, the n agents are evaluated simultaneously. The optimiser environment is coded on Python, and the parallelism is done with the MPI standard using the mpi4py package [21]. Every iteration takes about 3 hours to be completed, and an average of 96 hours is necessary when the maximum number of iterations are performed.

Although the response surface is not discrete, limitations regarding the element size constraint the results as noted on section 2.2.2. According to previous tests, geometrical resolution is at the order of $0.001d$, what traduces to the fact that for of any parameter, variations smaller than 0.001 will not result in a different solid domain. Consequently, to avoid unnecessary simulations, at the time the solver is called, the values of the geometrical parameters are rounded to the third decimal. In the case of recurrent calls to a previously simulated configuration, the former result is reused in the optimisation routine.

Though convergence of aerodynamic quantities in time are measured in real-time for each simulation, it was observed that the behaviour is errant when different geometries are compared, leading to premature or retarded simulations stops when convergence criteria is used. To avoid an excessive number of idle processors in the optimization run, rather than defining a stop criteria, the number of flow cycles is constant for all cases and sufficient for a good convergence ($t = 360 \times d/U_\infty$, up to 50 lift cycles). According to the convergence curve presented on Figure 5, obtained precision of time solution is at order of 0.010%.

3.2 Parametrized geometry

Final component of the shape optimisation routine is the geometry. A low order parametric approach is employed, where a fine control of geometrical characteristics is not possible. This choice is coherent both with the chosen optimizer and to the fact that small nuances of the geometry are not relevant for the final flow equilibrium for the regime in study, as presented in section 2.2. In that sense, consequential shape modifications are expected in the search of geometries that present extreme aeroacoustical quantities.

Test geometry is a polygonal section, defined by 4 control points positioned in the edges of a circumscribing rectangle. With respect to the parametrisation used in [8], we aim at enlarging the varieties of aeroacoustic answers, here enabling non-zero mean lift and a simpler flow dynamics by fixing detachment at edges.

The dimensional parameters are the height d and the aspect ratio $AR = L/d$; four non-dimensional parameters, each in [0,1], define the distance of a control point and the origin of its containing edge in the outer rectangle, always in the axis direction: upstream edge ratio (k_u), downstream edge ratio (k_d), top edge ratio (k_t) and bottom edge ratio (k_b), as illustrated in 7, and define a point in the design space $P_4 = (k_u,k_d,k_t,k_b)$ for a selected rectangle (d, AR). Different combinations of those 4 parameters produce triangles, rectangles, lozenges or any other polygonal section with 4 edges. Once the height is fixed for constant blockage ratio, optimisations are performed up-to 5 dimensions.

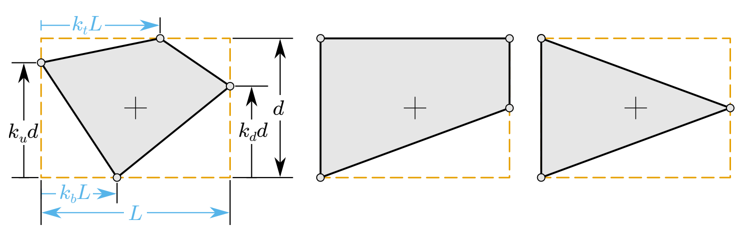

Figure 7: Scheme of the parametrized geometry (left) and examples of the possible geometries: $P_4 = (1.0, 0.5, 1.0, 0.0)$, center, and $P_4 = (0.0, 0.5, 0.0, 0.0)$, right.

Due to the nature of the parametrization, there are at least two points in the design space that produce the same geometry when shape is mirrored in y_1 axis, and would produce the same aeroacoustical outcome, only with reverse mean lift, for example, $P_4 = (0.5;\ 0.3;\ 0.2;\ 0.0)$ and $P_4 = (0.5;\ 0.7;\ 0.0;\ 0.2)$. This property guarantees that there are at least 2 global minimums, what is not accounted in the conception of the optimisation routine. The effects of having such characteristic in the response surface is not checked and there is no inspection step to avoid that such duplicates are evaluated twice.

4 Results

In the search to investigate the mechanisms associated with the tonal noise generated by a flow, shapes that present both the minimum and the maximum values are of interest. Therefore, for different quantities ($|C_D|$, C'_L and W), optimisation routine was employed for minimisation and maximisation (minimizing the inverse).

Besides the use of PSO, a technique already more adapted to complex response function than gradient based optimisers, there are no extra efforts to mitigate the chances to converge in local minima, such as more restraining topologies. For some optimisations performed for this study, there were clear indications that the obtained geometries were not the global minimum, either from the attained value or from the related form. In those cases, the optimisation was relaunched from the beginning and the final value was compared to the previous answer and only the best (the values that are considered global minima or maxima) are presented.

Pairs of optimal shapes and their corresponding aerodynamic quantities are listed on Table 2, where the cost/objective value are in bold; the normalized acoustic power, $W_a = W/(d\rho_0 U_\infty^3)$, is presented. Graphical representation of the obtained shapes is available at Figure 8, while flow and geometry aspects are discussed on the following sections.

As can be seen on the obtained geometrical parameters, at least 2 of the 4 edge ratios were always on the limits of the design space (either 0 or 1). It is observed that, after a few iterations, these final values are already selected and the search is reduced to a 3D or 2D design space. In terms of the optimisation procedure, the search for the best response is facilitated, however, it shows that the choice of the parametrization may be poor, once only a part of the variables retain the control of the cost function. In terms of the physics of the problem, it means that for a fixed height, the angle of the facing edge is the least significant in both the noise and the mean drag characteristics of an obstacle.

Table 2: Optimisation results.

objective	AR	k_u	k_d	k_t	k_b	$\|C_L\|$	$\|C_D\|$	C'_L	C'_D	St	$W_a \times 10^5$
min $\|C_D\|$ *	1.000	0.113	1.000	0.000	1.000	0.153	**1.274**	0.220	0.017	0.180	1.72
max $\|C_D\|$ *	1.000	0.946	0.000	0.000	0.882	1.614	**2.259**	0.458	0.127	0.181	8.60
min C'_L *	1.000	0.935	0.000	1.000	0.000	-0.038	1.288	**0.210**	0.013	0.174	1.52
max C'_L *	1.000	1.000	0.275	0.000	0.242	0.391	2.258	**1.058**	0.201	0.171	40.17
min W_a *	1.000	0.959	0.000	1.000	0.000	-0.005	1.311	0.211	0.010	0.171	**1.50**
max W_a *	1.000	1.000	0.285	0.000	0.201	0.330	2.233	1.055	0.195	0.172	**40.22**
min W_a +	2.000	1.000	0.111	0.956	0.000	-0.062	1.127	0.101	0.002	0.165	**0.33**
max W_a +	1.100	1.000	0.279	0.000	0.234	0.331	2.117	1.066	0.186	0.164	**38.79**

*: fixed AR; +: AR as a parameter in the optimisation, $AR \in [0.5, 2.0]$.

Obtained values for rectangles at different lengths are presented on Table 4 and serve as a reference for comparison with the optimal sections. Due to the symmetry, mean lift is null, so omitted from the table.

Table 3: Aerodynamic quantities for a rectangular section.

AR	$\|C_D\|$	C'_L	C'_D	St	$W_a \times 10^5$
0.500	1.895	0.572	0.077	0.193	12.83
1.000	1.347	0.223	0.011	0.167	8.63
2.000	1.138	0.119	0.002	0.164	0.45

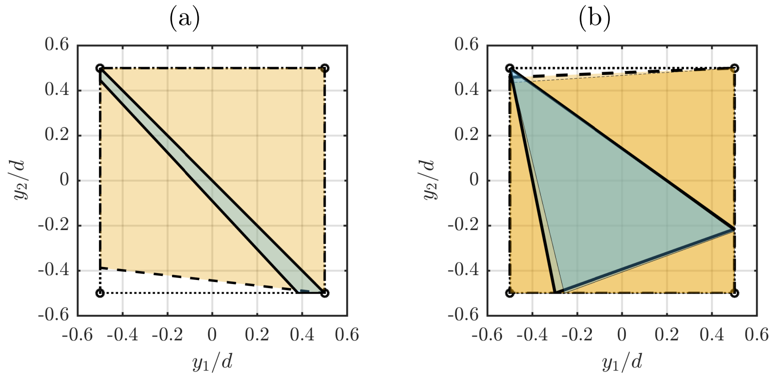

Figure 8: Optimal geometry at fixed $AR = 1.0$, dotted line is the containing rectangle. (a) minimum $|C_D|$ (dashed line) and maximum $|C_D|$ (solid line); (b) minimum C'_L (thick dashed line) and W (thin dashed line) and maximum C'_L (thick solid line) and W (thin solid line).

4.1 Mean drag

The resulting extrema of drag are associated with fairly different geometries. A range of $\Delta[C_D|$ that equals 73% of the drag of the square cylinder is obtained. Although the viscosity effects are not negligible for the selected flow conditions (Sheard at al. [15] presented that 21% of the drag was from the viscous shear tensor for a square cylinder at the same regime), pressure forces remain the major influence of the drag. From a preliminary analysis, the obtained velocity fields do not vary much, thus viscous efforts are not discussed here. The pressure field for the optimal pair and the square are illustrated on Figure 9.

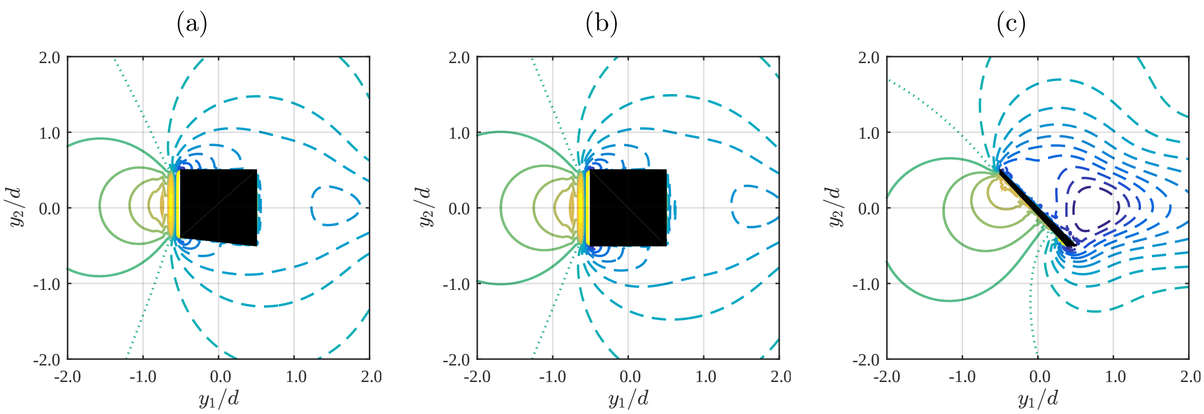

Figure 9: Mean pressure field for (a) minimum drag shape, (b) square and (c) maximum drag shape. Pressure coefficient contour, interval of 0.1. Continuous line for positive, dashed line for negative and dotted line for null.

Minimum drag geometry, Figure 9.a, is a slightly distorted square, with the bottom edge elevated at the upstream portion. The resulting flow is slightly asymmetrical, and when compared to the rectangle the mean drag is reduced by 5.4%. There is a decrease in the surface submitted to the frontal over pressure, and once the bottom edge normal has a component in the streamwise direction, the depression on this edge also contributes to drag reduction.

The biggest drag in encountered for a flat plate like geometry, Figure 9.c. The changes in the level of vorticity are small, however, the modification in the disposition of the vortex in the wake created an important depression zone downstream of the section that overcomes the reduction on the pressure on the upstream face. It's known that the drag only increases with the angle of attack of a plate, however, at a constrained aspect ratio, this is the biggest angle possible.

For the latter shape, the result is doubted due to the reduced number of solid points, with some horizontal slices (in the streamwise direction) of the body having only one solid element. The numeric scheme is of order 6, so downstream parts of the flow were being directly influenced by the flow upstream of the obstacle, what is non-physical. To check the consistency of the solution, simulation is re-run with mesh 4, where slices with single or double solid elements only exist in extreme upper part of the discrete shape. There are no significant changes in the flow, but small variations in the aerodynamic quantities are obtained: -2.6% of mean lift, -9.4% of mean drag, +0.9% of RMS lift and + 21.9% of RMS drag and -0.7% of St. However, specially for the aimed quantity, the original value are of the same order and consistently higher than the minimum, reinforcing that the optimisation result and the numerical setup are reasonable.

4.2 Fluctuating lift and acoustic power

As presented on Table 2, minimum/maximum RMS lift and acoustic power are searched independently. As noted on their geometrical parameters and aerodynamic results, the obtained geometries are quite similar, see Figure 8, and aeroacoustical differences may be considered within the precisions of the calculations. Thus only the results for the acoustic power are going to be described in details. Even so the answer are virtually identical, it is noted that the RMS lift is still better when it is the objective function than when the latter is the acoustic power, and vice versa, and this constitutes a sign of the success of the optimisation procedures.

The similarity of these result corroborates with the fact that the transverse fluctuations of the flow, incorporated in the fluctuating lift, are the most important element in the description of the tonal noise of 2D bluff bodies. Based on the equation used as the acoustic model on this work, remaining variables are the Mach number, C_D' and St. The compressibility effects (M) are unchanged between the geometries due the use an incompressible source at fixed flow conditions. For the second variable, it remains one order lower than the fluctuating lift. Interestingly, when comparing the minimum and the maximum, the increase of C_D' is as twice as big. That means that even if the drag contribution to the noise remains small, it has a wider range and thus is more affected by modifications in the obstacle's shape. For the St number, there is a really small variation of its value for the set of geometries evaluated in this study, what can be associated with the fixed height and the limitations regarding geometry modification. Due to those constraints, the width of the wake, the main feature to control its frequency [22], is only moderately modified, keeping St rather unchanged (around 0.17 ± 0.1).

It is important to note that both fluctuating quantities followed the same trend as the mean drag. However, as can be noted on the listed results, there is no direct association between them, being the drag for the minimum acoustic power higher than the minimized drag.

Vorticity snapshots for both minimum and maximum and the rectangle of same aspect ratio (square) are presented at Figure 10.

Similarly to the previous minimizing geometry, the minimum W is associated with a deformed square. For this case, the upper edge is lowered at the upstream portion, close to a mirrored version of the previous case. The obtained answer is only -0.37 dB quieter than the square, and is likely to be associated with a small increase of viscous dissipation on the top of the obstacle provoked by the enlargement of the boundary extension, what reflects in slightly weaker vortex.

The geometry that amplifies the noise power is a back-facing triangle. The interaction of both mixing layers is increased, what results in shorter recirculation and formations lengths, and simultaneously stronger vortex, as presented on Figure 10.c. The interaction of those structures with the walls of the obstacle causes larger C_D' and C_L', while the Strouhal number is only slightly modified. The wake remains symmetrical, but the symmetry axis is angled towards the upper boundary. This would must certainly modify the directivity of the sound, but the evaluation of this aspect of the acoustical field is not available from the tools used in this work and does not affect the total acoustic power.

Optimisations of the acoustic power at 5 degrees of freedom (DoF) are also performed, for the AR in [0.5; 2.0], and the obtained shapes are illustrated on Figure 11.a. As for the previous cases, a deformed rectangle is obtained for minimum W, for the longest geometry possible. In this case, the deviation is on the other sense, at the downstream portion of the bottom edge. From the observation of vorticity fields of the shape with minimal noise and the rectangular section of $AR = 2.0$, it is believed that, at that length, the small modifications in the lateral edge's angle are close to insignificant when compared to the effect of the length itself and further investigation of that influence are performed.

Figure 11.b illustrates the obtained acoustic power for all the points evaluated in the 2 optimisation

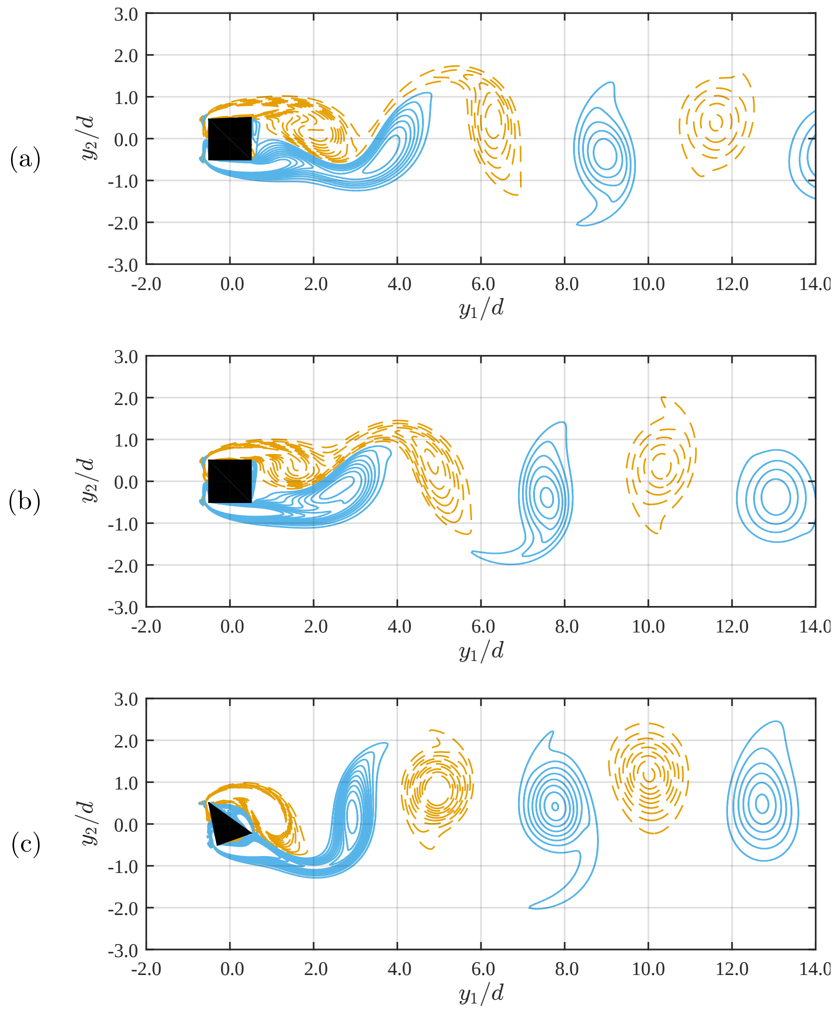

Figure 10: Snapshots of vorticity for (a) minimum acoustic power shape, (b) a square and (c) maximum acoustic power shape, interval of 0.3 U_∞/d. Continuous line for positive and dashed line for negative.

runs with the aspect ratio as a parameter and partially reproduces the values obtained for rectangular sections presented at Section 2.2.4. There's a clear association between the length and the acoustic power, indicating that it's rather a global trend, independent of the form of the geometry, that can be associated to the reduction of the interaction between the mixing layers and the weakening of the vortex by viscous dissipation for longer sections. We may also conclude that the rectangles are already fairly optimal sections in terms of noise production.

The maximum noise is obtained with another triangle, but not in the minimum aspect ratio. The resulting length is a compromise between flow fluctuations and the available surface to transform that in lift oscillations, similarly to the behaviour noted by Inasawa et al. [17]. It must also be pointed out that the alterations of the aspect ratio were capable of substantially modifying the frequency of the wake, thus, provoking a larger discrimination between the minimum and the maximum noise than what was obtained at fixed AR.

As can be seen on table 2, the maximum noise obtained for the 5 DoF optimisation ($W_a = 38.79 \times 10^{-5}$) is lower than the value obtained ate fixed length ($W_a = 40.22 \times 10^{-5}$). As clarified previously, some optimisations are believed to converge to local minima, and it was the case for the maximum noise. The same configuration was optimized 3 times, starting for a design space of $AR \in [0.5; 2.0]$ for the aspect ratio for the first two runs and [0.75; 1.25] for the final one, and even so the final result is clearly not the global

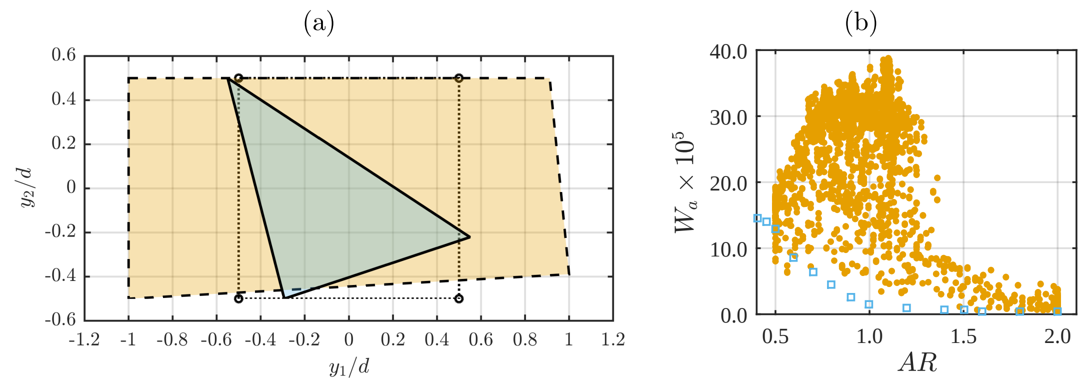

Figure 11: Acoustic power for different geometries as a function of their length. Dots include all the geometries evaluated for the 5 DoF optimisations and square makers are for rectangles.

minimum. The obtained misbehaviour contributes to the conclusion that, for every geometry (associated to an specific P_4 coordinates point), there is a unique length that maximizes the noise, in such a way that there are multiple local minimum in the design space. Besides the use of a different swarm topology, a re-setting of the number of particles, total number of iterations and the optimisation coefficients could ameliorate the result.

Even for a very limited set of tested geometries at a fixed blockage ratio, globally, a ratio of 2 for the mean drag and a rapport of 20 dB for the noise is observed between the extrema. Modifications of the upper and lower edges are the most active in terms of the aerodynamic and aeroacoustic answers. Although the large range, all the obtained results are originated by similar wakes.

5 Conclusions

An optimization routine based on a stochastic technique is presented for tonal noise of a compact source. The geometry is an infinite span cylinder with a polygonal section modelled by an IBM approach; the acoustics is calculated by a single formula model issued from a Curle's analogy, alimented by the results of an incompressible aerodynamic solver at $Re = 150$.

The feasibility of the performed optimisation procedure relays fundamentally on the robustness of both the optimizer (PSO) and the IBM. In that way, the management of the tested geometries was possible without direct interference after both optimisation and flow simulation settings were defined in careful preliminary studies. Simultaneously, the use of an hybrid acoustic model that is capable of representing the acoustic from global flow statistics was an essential component of the proposed framework.

From the obtained optima, it is clear that the key to reduce the noise production is to decrease the strength and the interaction between the top and bottom shear layers in the wake of a bluff body, such that long or bluffer geometries, therefore, the ones where the interactions of the mixing layers is reduced, are the ones with smallest C'_L and consequently lower acoustic power. The result is aligned with the canonical experiment with a splitter plate by Roshko [23] and its repercussions. At fixed height and length, that reduction was obtained with small increase of one of the lateral edges of the geometry and thus increase viscous dissipation of the forming vortex. From tests with a modifiable length, the aspect ratio is concluded to be the most important factor for reducing the noise. On the other way, maximum acoustic power is associated with back facing triangles, where the effect is inverted: more interaction between the layers and stronger vortex on the wake.

A correlation between the acoustic power and the mean drag is also implied, being the biggest drag always associated with a large C'_L and vice-versa, what is believed to be due to the association of base suction and wake instability [1]. The Strouhal number oscillates unsubstantially, as it's more associated with the wake width, a property relatively fixed from the geometrical constraints used on this work.

Another interesting comportment that outlays with the associations of mean drag and fluctuating lift, is that, when one of them is aimed, the other may not be the optimal at the end of the optimisation. Setting the square as reference, when aiming for minimum noise there is a reduction of 2.7% of the drag. Oppositely, when searching for minimum drag, there is a 0.23 dB increase of acoustical noise. Although this conclusion is limited to the regime and the characteristics of the test geometry, this is a rather dangerous trend, once the aeroacoustic is most commonly neglected in face of the drag, that touches directly the aerodynamic performance.

It is observed that, under the limitations of both the space discretization and the geometry complexity, modifications that increase or decrease the acoustic emission are fundamentally associated with modifying the RMS lift. Besides the known fact that it's the fundamental fuel for bluff body noise, the incapacity of the geometry to influence the other parameters in the acoustic model at the same impact, such as the Strouhal number and the fluctuating drag, is an important conclusion regarding not only the acoustics, but eventual applications on energy harvesting.

References

[1] A. Roshko. Perspectives on bluff body aerodynamics. *Journal of Wind Engineering and Industrial Aerodynamics*, 49(1):79 – 100, 1993.

[2] E.M. Papoutsis-Kiachagias, N. Magoulas, J. Mueller, C. Othmer, and K.C. Giannakoglou. Noise reduction in car aerodynamics using a surrogate objective function and the continuous adjoint method with wall functions. *Computers & Fluids*, 122:223 – 232, 2015.

[3] S. B. Yao, D. L. Guo, Z. X. Sun, D. W. Chen, and G. W. Yang. Parametric design and optimization of high speed train nose. *Optimization and Engineering*, 17(3):605–630, 2016.

[4] S. Becker, C. Hahn, M. Kaltenbacher, and R. Lerch. Flow-induced sound of wall-mounted cylinders with different geometries. *AIAA Journal*, 46(9):2265–2281, September 2008.

[5] W. F. King and E. Pfizenmaier. An experimental study of sound generated by flows around cylinders of different cross-section. *Journal of Sound and Vibration*, 328(3):318–337, 2009.

[6] Y. Oguma, T. Yamagata, and N. Fujisawa. Measurement of sound source distribution around a circular cylinder in a uniform flow by combined particle image velocimetry and microphone technique. *Journal of Wind Engineering and Industrial Aerodynamics*, 118:1 – 11, 2013.

[7] N. Curle. The influence of solid boundaries upon aerodynamic sound. *Proceedings of the Royal Society of London A: Mathematical, Physical and Engineering Sciences*, 231(1187):505–514, 1955.

[8] W. J. G. S. Pinto and F. Margnat. A shape optimization procedure for cylinders aeolian tone. *under consideration for publication in Computer & Fluids*, 2018.

[9] F. Margnat. Hybrid prediction of the aerodynamic noise radiated by a rectangular cylinder at incidence. *Computers and Fluids*, 109(4):13–26, 2015.

[10] S. Laizet and E. Lamballais. High-order compact schemes for incompressible flows: A simple and efficient method with quasi-spectral accuracy. *J. Comp. Phys.*, 228:5989–6015, 2009.

[11] D. Goldstein, R. Handler, and L. Sirovich. Modeling a no-slip boundary condition with an external force field. *J. Comp. Phys.*, 105:354–366, 1993.

[12] F. Margnat and V. Morinière. Behavior of an immersed boundary method in unsteady flows over sharp-edged bodies. *Computers and Fluids*, 38(6):1065–1079, 2009.

[13] A. Sohankar, C. Norberg, and L. Davidson. Low-reynolds-number flow around a square cylinder at incidence: study of blockage, onset of vortex shedding and outlet boundary condition. *International Journal for Numerical Methods in Fluids*, 26(1):39–56, 1998.

[14] O. Posdziech and R. Grundmann. A systematic approach to the numerical calculation of fundamental quantities of the two-dimensional flow over a circular cylinder. *Journal of Fluids and Structures*, 23(3):479 – 499, 2007.

[15] G. J. Sheard, K. Hourigan, and M. C. Thompson. Computations of the drag coefficients for low-reynolds-number flow past rings. *Journal of Fluid Mechanics*, 526:257Ű275, 2005.

[16] L. Qu, C. Norberg, L. Davidson, S.-H. Peng, and F. Wang. Quantitative numerical analysis of flow past a circular cylinder at reynolds number between 50 and 200. *Journal of Fluids and Structures*, 39(Supplement C):347 – 370, 2013.

[17] A. Inasawa, M. Asai, and T. Nakano. Sound generation in the flow behind a rectangular cylinder of various aspect ratios at low mach numbers. *Computers & Fluids*, 82(Supplement C):148 – 157, 2013.

[18] R J. Kennedy and Eberhart. Particle swarm optimization. In *Proceedings of IEEE International Conference on Neural Networks IV, pages*, volume 1000, 1995.

[19] R. Poli, J. Kennedy, and T. Blackwell. Particle swarm optimization. *Swarm Intelligence*, 1(1):33–57, Jun 2007.

[20] I. C. Trelea. The particle swarm optimization algorithm: convergence analysis and parameter selection. *Information Processing Letters*, 85(6):317 – 325, 2003.

[21] L. Dalcín, R. Paz, M. Storti, and J. D'Elía. Mpi for python: Performance improvements and mpi-2 extensions. *Journal of Parallel and Distributed Computing*, 68(5):655 – 662, 2008.

[22] A. Roshko. On the wake and drag of bluff bodies. *Journal of the Aeronautical Sciences*, 22(2):124–132, February 1955.

[23] A. Roshko. On the drag and shedding frequency of two-dimensional bluff bodies. Technical report, National Advisory Committee for Aeronautics, 1954.